Article

Bilayer and Trilayer C₃N/Blue-Phosphorene Heterostructures as Potential Anode Materials for Potassium-Ion Batteries

Ali Khodadadi, Akhil Kunjikuttan Nair, Carlos Manuel Da Silva, and Cristina H. Amon*
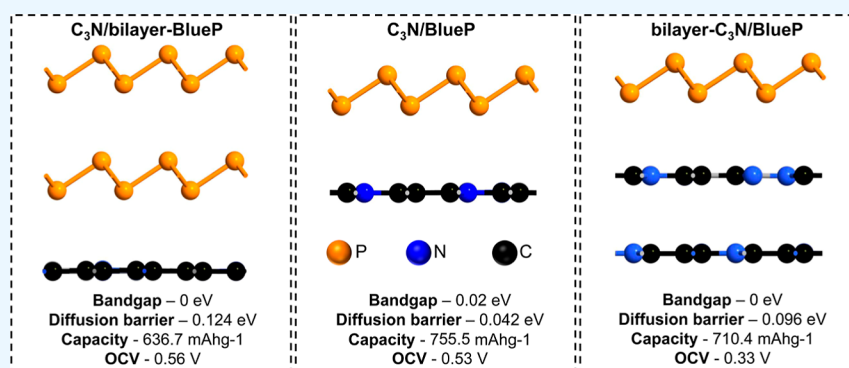
Read Online

ACCESS | 📊 Metrics & More | 📖 Article Recommendations | 🆂🅸 Supporting Information

ABSTRACT: Two-dimensional (2D) van der Waals heterostructures outperform conventional anode materials for postlithium-ion batteries in terms of mechanical, thermal, and electrochemical properties. This study systemically investigates the performance of bilayer and trilayer C₃N/blue phosphorene (C₃N/BlueP) heterostructures as anode materials for potassium-ion batteries (KIBs) using first-principles density functional theory calculations. This study reveals that the adsorption and diffusion of K ions on bilayer and trilayer C₃N/BlueP heterostructures are markedly superior to those of their monolayer counterparts. A bilayer heterostructure (C₃N/BlueP) effectively reduces the bandgap of the BlueP monolayer (1.98 eV) to 0.02 eV, whereas trilayer heterostructures (bilayer-C₃N/BlueP and C₃N/bilayer-BlueP) exhibit metallic behavior with no bandgap. Additionally, the theoretical capacity of the bilayer and trilayer heterostructures ranges from 636.7 to 755.5 mA h g^{-1}, considerably higher than the theoretical capacity of other prospective 2D heterostructures for KIBs investigated in the literature. This study also shows that the heterostructures exhibit K-ion diffusion barriers as low as 0.042 eV, ensuring the relatively fast diffusion of K ions.

1. INTRODUCTION

There has been significant interest in potassium-ion batteries (KIBs) as a cost-effective energy storage technology with comparable energy densities to lithium-ion batteries (LIBs). KIBs can offer more competitive prices than LIBs due to the abundance of potassium ions in the earth's crust (e.g., the potassium/lithium concentration of 28650/22 ppm in the upper continental crust), which reduces mining costs.[1] Additionally, they are more suitable for high-voltage applications than other alternatives, such as sodium-ion batteries (NIBs), due to the K/K⁺ system's low standard electrode potential.[2] Despite these advantages, KIBs continue to exhibit lower capacity ranges compared to LIBs due to the lack of suitable anode materials. Selecting anode materials capable of reversibly storing K ions is challenging due to the large radius of K ions, which leads to high volume expansions. In large-volume expansions, the anode material is susceptible to pulverization, which can result in the detachment of the anode material from the current collectors and poor cycling stability.[3]

The battery research community has conducted many studies to discover appropriate anode materials for KIBs. Most recently, 2D materials, including elemental monolayers (such as blue phosphorene[4]), compound materials (such as C₃N[5]), transition metal dichalcogenides[6−8] (such as WS₂[9] and MoS₂[10]), and transition-metal-doped 2D materials[11−13] and heterostructures[14] have received considerable attention. These materials may often adsorb a large number of K ions due to their high surface-to-volume ratio. For example, C₃N and blue phosphorene monolayers exhibit theoretically specific capacities of 1072,[5] and 865 mA h g^{-1}[4] for KIBs, respectively. Among monolayers, blue phosphorene (BlueP), which was demonstrated theoretically in 2014[15] and synthesized in

2016,[16] has attracted considerable interest in the battery research community. BlueP is as stable as a monolayer of black phosphorene (BlackP) and exhibits intriguing properties. According to theoretical calculations, BlueP has a higher storage capacity and a lower diffusion barrier for lithium and postlithium ion batteries than BlackP.[4] However, the large 1.95 eV bandgap of BlueP precludes it from being used in batteries, in which rapid electron transport is crucial for maximizing performance and minimizing susceptibility to temperature-induced degradation phenomena.[4] A practical solution to overcome these limitations is to create 2D heterostructures by stacking suitable monolayers on top of BlueP.

Monolayer C_3N, a graphene-like 2D crystal consisting of carbon and nitrogen atoms, is considered one of the ideal candidates for forming an alternating structure due to its promising electronic properties, ultrahigh stiffness, high thermal conductivity, and stability at high temperatures.[17,18] The strong electronegative nitrogen atoms in C_3N facilitate electrochemical interactions between positive metal ions and the C_3N layer. However, these atoms decrease ion diffusion coefficients, rendering the C_3N layer unsuitable for use as an anode material in metal-ion batteries.[18]

Heterostructures of alternating 2D monolayers of C_3N/C_3B, $C_3N/BlackP$, and $C_3N/BlueP$ have recently gained much attention as promising anode materials for metal-ion batteries as they can compensate for the shortcomings of their monolayer counterparts.[19−21] For instance, it has been demonstrated that $C_3N/BlueP$ heterostructures significantly reduce the electronic bandgap and improve Li-ion diffusion coefficients, which are the primary limitations of BlueP and C_3N monolayers.[21] Bao et al.[22] theoretically investigated the electrochemical properties of $C_3N/BlueP$ heterostructures and reported storage capacities of 363.74 and 1510.95 mA h g^{-1} for LIBs and NIBs, respectively. Theoretical studies typically evaluate the electrochemical properties of 2D heterostructures by stacking two monolayers on top of each other. However, from an experimental perspective, stacking monolayers on top of each other to fabricate a bilayer material is challenging, making it technically difficult to experimentally verify the density functional theory (DFT) results at this low dimensionality. It has been demonstrated that manufacturing 2D materials using cost-effective experiments does not necessarily produce a uniform material with a constant thickness throughout the sample.[23−26] Therefore, it is more likely that the fabricated product will be a mixture of heterostructures with varying numbers of layers. There is strong evidence that the number of layers significantly affects the properties of materials. For instance, it has been found that bulk WS_2 adsorbs about 30% fewer K ions than monolayer WS_2, meaning the capacity of its monolayer is around 30% more than that of its bulk form.[9] Therefore, evaluating the effect of the number of layers on the electrochemical properties of 2D heterostructures is essential to bridging the gap between simulations and experiments. This will help theoretical researchers report a range of values that can be achieved by conducting experiments.

This study evaluates the electrochemical properties of bilayer and trilayer $C_3N/BlueP$ heterostructures as anode materials in KIBs by using DFT simulations. We first assess the room-temperature stability and electronic properties of three heterostructures, namely, monolayer-C_3N/monolayer-BlueP ($C_3N/BlueP$), bilayer-C_3N/monolayer-BlueP (bilayer-C_3N/BlueP), and monolayer-C_3N/bilayer-BlueP (C_3N/bilayer-

BlueP) heterostructures. We then identify the most favorable intercalation sites by calculating and comparing adsorption energy values. Afterward, we evaluate the charge density difference contours, a technique for determining the nature of the intercalated atom's bonds with the substrates. In addition, the Bader charge analysis is used to quantify the charges transferred between the K ion and the substrate.[27] Furthermore, climbing image-nudged elastic band (CI-NEB) simulations are conducted to estimate the diffusion energy barriers associated with K-ion passage through the heterostructures. Finally, we determine the most significant features of electrode materials, i.e., open-circuit voltages (OCVs) and theoretical capacities. This study shows that $C_3N/BlueP$ heterostructures are excellent anode materials for KIBs. Additional experimental research outside the scope of this study is recommended to further evaluate the electrochemical performance of the $C_3N/BlueP$ heterostructures.

2. COMPUTATIONAL METHODS

All DFT calculations were carried out using the Quantum Espresso package based on the Perdew−Burke−Ernzerhof exchange−correlation functional.[28,29] While the optimized norm-conserving Vanderbilt pseudopotentials were used to perform all simulations, including electronic band structure and the intercalation energy calculations,[30] the projected augmented-wave (PAW) pseudopotentials were used for the Bader charge analysis. A sizable kinetic energy cutoff of 70 Ry was used for the plane-wave expansion. This kinetic energy cutoff, higher than those typically applied (~500 eV), enables the accurate prediction of adsorption energy and the generation of higher-quality electronic band structures and densities of states. The Grimme (DFT-D2) scheme accounted for dispersion-corrected van der Waals interactions,[31] a highly efficient correction scheme for most materials, including the Li-graphite system.[32,33] The positions of atoms were optimized using the Broyden−Fletcher−Goldfarb−Shanno method.[34] Monkhorst−Pack grids[35] of 3 × 3 × 1 and 13 × 13 × 1 k-points were used for sampling the Brillion zone in the intercalation energy and electronic structure calculations, respectively. The geometry optimization convergence criteria were set to 1 × 10^{-3}, 1 × 10^{-4}, and 1 × 10^{-6} Ry for force, energy, and self-consistent calculations, respectively. A vacuum of 20 Å was considered in the out-of-plane direction to prevent interactions with periodic images. For visualization and postprocessing purposes, both the XCrysden[36] and VESTA[37] packages were used.

The first step in investigating 2D heterostructures is to identify their most stable stacking orientation. To this end, we need to calculate the formation energies of different stacking orientations and select the one with the lowest formation energy, which can be calculated as

$$E_{formation} = \frac{E_{hetero} - E_{C_3N} - E_{BlueP}}{N} \qquad (1)$$

where E_{hetero}, E_{C_3N}, E_{BlueP}, and N represent the total energy of the heterostructures, the total energy of the C_3N monolayer, the total energy of the BlueP monolayer, and the total number of atoms in the heterostructure, respectively. In the same way, the most favorable adsorption sites can be identified by calculating and comparing the average adsorption energies (E_{avg}) as
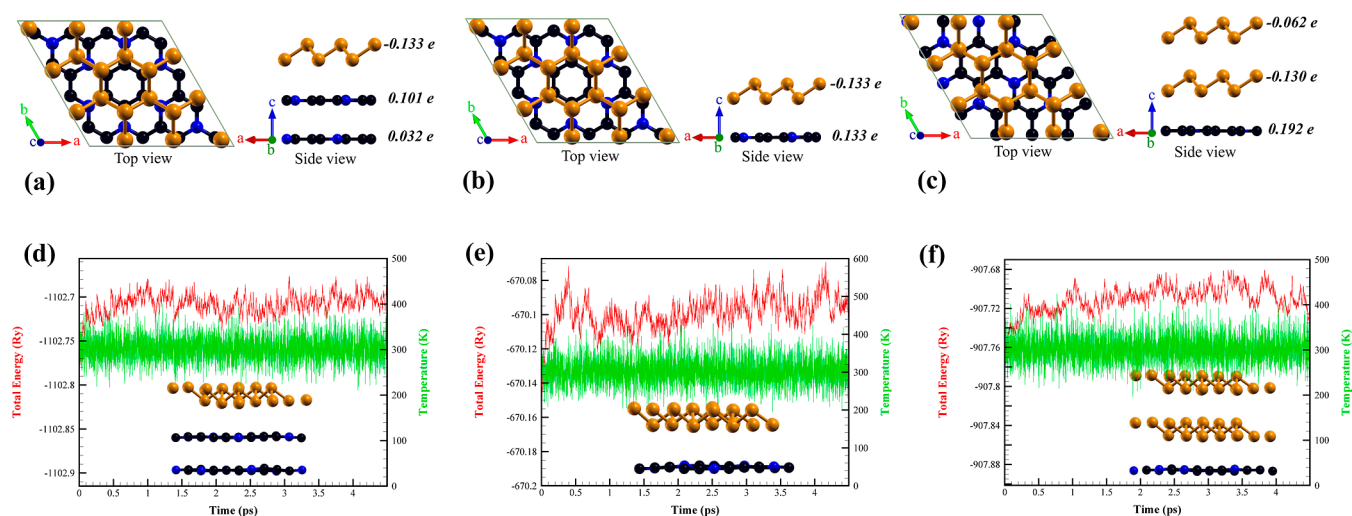
Figure 1. Top and side views of the most stable stacking orientations of the (a) bilayer-C_3N/BlueP, (b) C_3N/BlueP, and (c) C_3N/bilayer-BlueP heterostructures, along with each layer's charge transfers. The orange, black, and blue colors represent the phosphorene, carbon, and nitrogen atoms. The total energy and temperature profiles of (d) bilayer-C_3N/BlueP, (e) C_3N/BlueP, and (f) C_3N/bilayer-BlueP heterostructures. They also include snapshots of the atoms at the end of each AIMD simulation.

$$E_{avg} = \frac{E_{hetero+K} - E_{hetero} - nE_K}{n} \quad (2)$$

where $E_K = -56.76$ Ry is the energy of an isolated K-ion, calculated using the spin-polarized DFT simulations, E_{hetero} is the energy of the substrate without any adsorbed ion, $E_{hetero+K}$ is the energy of the substrate with the adsorbed ions, and n is the number of adsorbed K ions. The negative adsorption energy leads to the formation of a stable and robust interaction between the adatom and the substrate, indicating that the K-ion is spontaneously adsorbed on the substrate.

Additionally, electrode materials are typically compared using their capacities and OCVs. They can also help determine appropriate state-of-charge levels to extend the battery's lifespan. The OCV can be determined by

$$OCV = \frac{E_{hetero+K} - E_{hetero} - n\mu_K}{en} \quad (3)$$

where e is the elementary charge and $\mu_K = -56.78$ Ry is the energy of the bulk potassium in the body-centered-cubic crystal form. Next, the theoretical specific capacity of the heterostructure is defined by

$$C = \frac{1000 \times nF}{M_{hetero}} \quad (4)$$

where F represents the Faraday's constant (26.80 Ah/mol), and M_{hetero} indicates the molecular mass of the heterostructure.

In order to evaluate the bonds formed between intercalated ions and the substrates, the charge density difference is calculated similarly to the adsorption energy by

$$\rho_{ad} = \rho_{adsorbedstate} - \rho_{substarte} - \rho_{adsorbent} \quad (5)$$

where $\rho_{adsorbed\ state}$ is the charge density of the structure after the intercalation of K ions, $\rho_{substarte}$ is the charge density of the substrates before intercalation, and $\rho_{adsorbent}$ is the charge density of an isolated K-ion.

3. RESULTS AND DISCUSSION

3.1. Lattice Structure and Thermal Stability of C_3N/BlueP Heterostructures.
Calculating the lattice constants of the BlueP and C_3N monolayers is the first step in constructing C_3N/BlueP heterostructures. Our computed lattice constants, 3.278 Å for BlueP and 4.858 Å for C_3N agree with previously reported values.[4,38] Figure S1 in the Supporting Information section depicts the optimized buckled honeycomb crystal structures and unit cells of the BlueP and C_3N monolayers. As shown in Figure S1, the atoms of the C_3N monolayer belong to a single atomic plane, while the BlueP monolayer is composed of two distinct atomic planes separated by a vertical distance of 1.235 Å, resulting in a puckered structure. The equilibrium lengths of the C–C, C–N, and P–P bonds are 1.40, 1.40, and 2.26 Å, respectively.

We generated the heterostructure unit cells using a 2×2 supercell of C_3N and a 3×3 supercell of BlueP monolayers, resulting in minimal lattice mismatches. Each heterostructure can have a variety of possible layer stacking orientations. It is crucial to theoretically determine the most stable and favorable ones because those are the most likely to occur during experiments.[39] The literature indicates that AA and AD stackings are the most favorable configurations for BlueP and C_3N bilayers, respectively.[40,41] While we relied on this information to choose the stacking configuration, we also determined the optimal orientation for stacking the BlueP and C_3N layers at their interface. To this end, as shown in Figure S2, we considered three distinct preoptimized layer stacking orientations for each heterostructure. All the structures were then subjected to structural relaxation of energy and force to determine the optimal stacking arrangement. In this work, we selected the heterostructure orientations, which yielded the lowest total energy and subsequently determined the interlayer distance.

The most stable stacking configurations are those with the lowest formation energy values. Thus, it is necessary to calculate and compare their formation energies. To this end, Table S1 summarizes the formation energy values, interlayer distances, lattice parameters, and resulting C–C, C–N, and P–P bond lengths for bilayer-C_3N/BlueP, C_3N/BlueP, and C_3N/bilayer-BlueP heterostructures and their corresponding monolayer structures. All formation energy values are negative, indicating that all three heterostructures are energetically
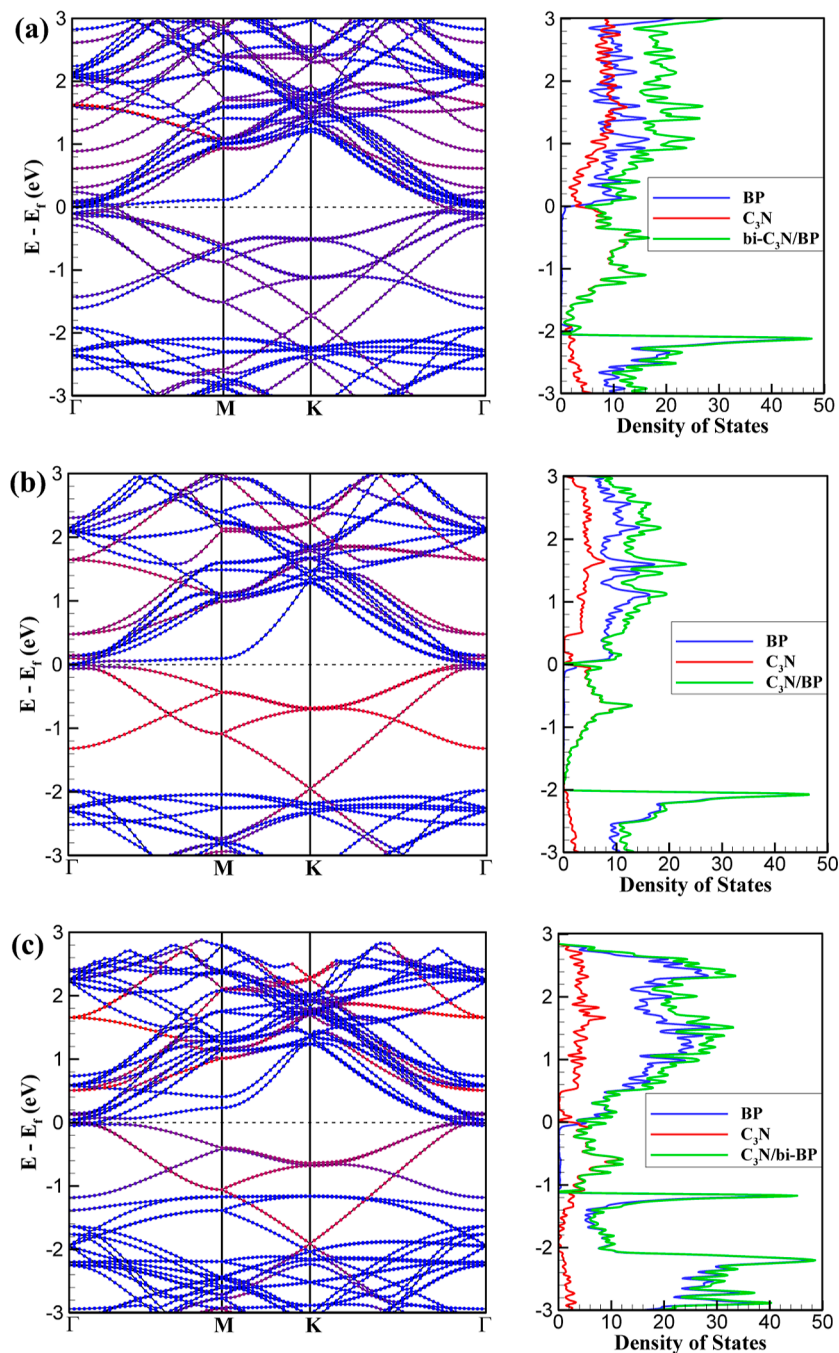
Figure 2. Projected electronic band structure and density of state plots of (a) bilayer-C_3N/BlueP, (b) C_3N/BlueP, and (c) C_3N/bilayer-BlueP heterostructures. The red and blue colors in the band structure plots show the contribution of the C_3N and BlueP layers to the overall band structure.

stable. However, structures in Figure S2a,e,k have the lowest formation energies for bilayer-C_3N/BlueP, C_3N/BlueP, and C_3N/bilayer-BlueP heterostructures, respectively. Hence, they are selected as the host structures for the remaining simulations and are shown in Figure 1a−c, respectively. These figures also include the charges gained or lost by each layer in these heterostructures, which are calculated using the Bader charge analysis. For example, C_3N layers gained a minimum/maximum of 0.032/0.192 electrons, while BlueP layers lost a minimum/maximum of 0.062/0.133 electrons. In addition, the maximum number of electrons gained by each C_3N layer increases as the number of BlueP layers increases,

while the maximum number of electrons lost by a BlueP layer remains nearly constant. This is because highly electronegative nitrogen atoms on the C_3N layers can attract electrons from BlueP layers far away from the C_3N layers, resulting in an increase in charge transfer.

In addition, our simulations demonstrated that the formation of heterostructures increases the C−C and C−N bond lengths and decreases the P−P bond lengths compared with those of the constituent monolayers. Therefore, the BlueP layer is subjected to compressive strain, whereas the C_3N layer is subjected to tensile strain. As the number of BlueP layers increases, the tensile strain decreases while the compressive

Table 1. Adsorption Energy, the Interlayer Distance, and the Charge Transfer (Q) Values of the K-Ion Intercalation Into the C_3N/BlueP Heterostructures

filling order	location	site	adsorption energy (eV)	interlayer distances		Q_K (e)	Q_{BlueP} (e)	QC3N (e)
				h_1 (Å)	h_2 (Å)			
1	C_3N/BlueP/K	T_{pd}	−1.60	3.34		0.84	−0.91	0.07
2	C_3N/K/BlueP	H_p	−1.13	4.24		0.82	−0.69	−0.13
3	K/C_3N/BlueP	H_c	−0.70	3.35		0.80	−0.37	−0.43
1	C_3N/C_3N/BlueP/K	T_{pd}	−1.60	3.20	3.35	0.84	−0.91	0.07
2	C_3N/C_3N/K/BlueP	H_p	−1.15	3.16	5.22	0.82	−0.58	−0.24
3	K/C_3N/C_3N/BlueP	H_c	−0.78	3.16	3.38	0.73	−0.19	−0.54
4	C_3N/K/C_3N/BlueP	H_p	−0.05	5.15	3.41	0.84	−0.26	−0.58
1	C_3N/BlueP/BlueP/K	T_{pd}	−1.83	3.44	3.11	0.85	−1.01	0.16
2	C_3N/BlueP/K/BlueP	H_p	−1.70	3.38	5.65	0.83	−0.95	0.12
3	C_3N/K/BlueP/BlueP	T_{pu}	−1.26	5.24	3.15	0.81	−0.70	−0.11
4	K/C_3N/BlueP/BlueP	H_c	−0.83	3.38	3.21	0.72	−0.37	−0.35

strain increases in the C_3N layers. According to the lattice parameters of the most stable configurations, there are only 1.05, 1.29, and 1.45% lattice mismatches, respectively, for bilayer-C_3N/BlueP, C_3N/BlueP, and C_3N/bilayer-BlueP, indicating their suitability for constructing the proposed heterostructures. Notably, the lattice constant and interlayer distance of the most stable configuration of the C_3N/BlueP heterostructure are 9.717 and 3.37 Å, respectively, which agree well with those reported in the literature.[21,22]

To evaluate the thermal stability of the heterostructures, we conducted ab initio molecular dynamics (AIMD) simulations for an extended period of 4.5 ps. Based on the total energy and temperature profiles shown in Figure 1, these materials are thermally stable at room temperature. As depicted in Figure 1d−f, the total energy exhibits relatively minor fluctuations in bilayer-C_3N/BlueP, C_3N/BlueP, and C_3N/bilayer-BlueP heterostructures, respectively, indicating that the atoms only oscillate in their equilibrium positions without any significant structural distortions.

We also calculated the heterostructures' four independent elastic constants, namely, C_{11}, C_{22}, C_{12}, and C_{44}, to establish the mechanical stability of the studied heterostructures. Table S2 contains these elastic constants for bilayer-C_3N/BlueP, C_3N/BlueP, and C_3N/bilayer-BlueP heterostructures, as well as their monolayer counterparts. The obtained elastic constants met Born's criteria for mechanical stability [42] defined as C_{11}, C_{22}, $C_{44} > 0$, and $C_{11}C_{22}−C_{12}^2 > 0$. It should be noted that the calculated elastic constants of the two-layer C_3N/BlueP heterostructure are well consistent with previously reported values.[21] Additionally, the heterostructures have isotropic in-plane mechanical properties based on the computed C_{11} and C_{22}. To further validate this conclusion and better understand the heterostructures' mechanical properties, the polar plots of their Young's moduli and Poisson's ratios are depicted in Figure S7, determined using a previously employed approach.[43] As can be seen in Figure S7a, the two-layer C_3N/BlueP heterostructure exhibits slightly anisotropic behavior. However, adding an extra BlueP or C_3N layer on top of the two-layer heterostructure reduces the in-plane anisotropy of its mechanical properties. Moreover, as depicted in Figure S7b, Young's moduli of all three heterostructures are significantly improved in all directions compared to those of monolayers. It is also evident that as the number of C_3N layers increases, Young's moduli of the heterostructures increase due to the superior mechanical properties of the C_3N monolayer compared to those of the

BlueP monolayer. Based on these findings, it is reasonable to conclude that combining monolayers resulted in a stable material with superior mechanical properties.

3.2. Electronic Properties of C_3N/BlueP Heterostructures. The projected electronic band structure and partial density of state plots (PDOS) of the C_3N/BlueP heterostructures are shown in Figure 2. As shown in Figure 2b, stacking the C_3N monolayer on top of the BlueP monolayer forms a semimetallic material with a bandgap of 0.02 eV, meaning its electronic conductivity is significantly higher than its monolayer counterparts (C_3N and BlueP monolayers have bandgaps of 0.38 and 1.98 eV, respectively, as shown in Figure S3). These properties are consistent with those reported in the literature.[21,22] On the other hand, Figure 2a,c shows that a C_3N or BlueP layer added on top of the bilayer heterostructure forms a metallic material, further enhancing the electronic conductivity.

3.3. Adsorption Properties of C_3N/BlueP Heterostructures. In the evaluation of an electrode material's electrochemical performance for KIBS, the binding strength between the K ion and the host material is of the utmost importance, which can be evaluated using adsorption energies. Generally, a K ion can be adsorbed on either side of each layer, namely the C_3N and BlueP layers. Therefore, three major adsorption locations exist in the bilayer C_3N/BlueP heterostructure: outside the BlueP layer, outside the C_3N layer, and between the layers. However, four major adsorption locations exist in trilayer C_3N/BlueP heterostructures: outside the BlueP layer, outside the C_3N layer, between the C_3N and BlueP layers, and at the interface of the C_3N or BlueP bilayers. Within each of these major adsorption locations, there are several sites where the K ion can be adsorbed stably.

We first placed the K ions at different sites at a reasonable distance from each other. Then, we allowed the system to relax and achieve the lowest total energy by conducting full geometry optimization. Similar to selecting the most favorable stacking orientation, the more negative adsorption energies belong to the more favorable adsorption sites. Table 1 summarizes the most favorable interlayer distances of adsorption sites, adsorption energies, and the gain/loss of electrons. In this table, the terms H and T stand for the center of hexagons and the top of any particular region, respectively. For example, H_c and T_d indicate that the K ion is located above the center of the carbon hexagon and the lower P atom, respectively. As shown, all adsorption energies are negative,
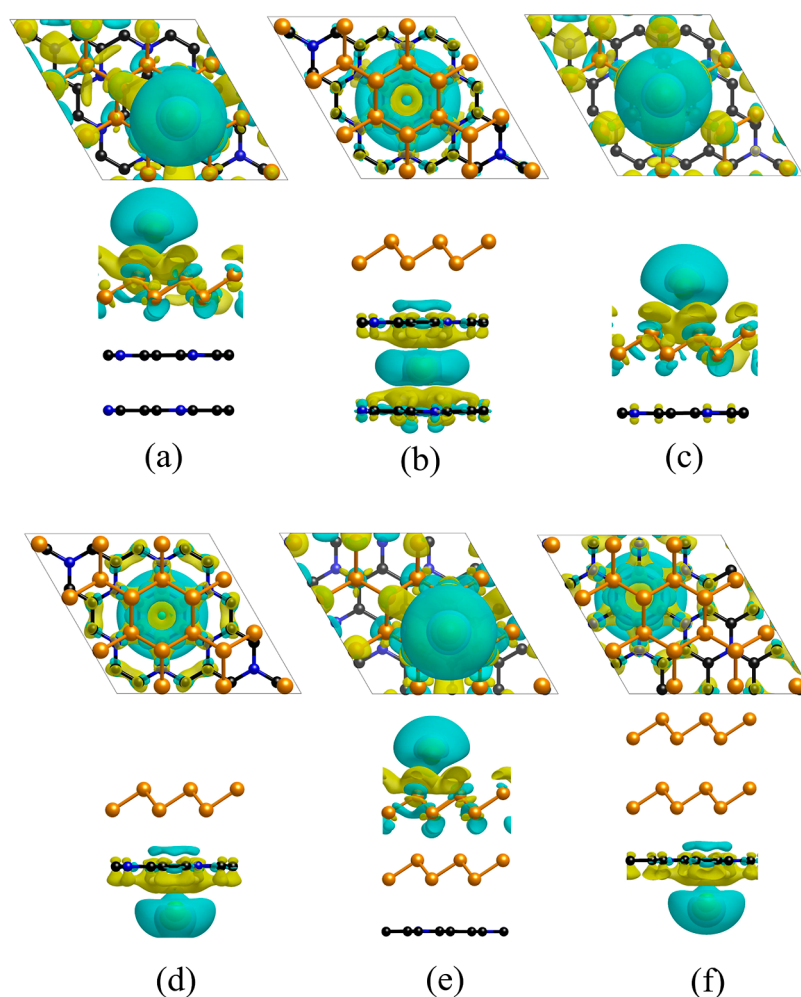
Figure 3. Charge density difference contours over the adsorption sites with the maximum and minimum charge transfers from a single K ion to (a,b) bilayer-C_3N/BlueP, (c,d) C_3N/BlueP, and (e,f) C_3N/bilayer-BlueP heterostructures. The isosurface level is set to 0.0006 e/Bohr^3. The cyan and yellow colors show the charge-depleted and -accumulated regions, respectively.

suggesting that the K-ion spontaneously intercalates into the structure without forming metal clusters.

Based on calculated adsorption energies, we can conclude that the most favorable sites are in the following order: C_3N/BlueP/K > C_3N/K/BlueP > K/C_3N/BlueP for the C_3N/BlueP heterostructure, C_3N/C_3N/BlueP/K > C_3N/C_3N/K/BlueP > K/C_3N/C_3N/BlueP > C_3N/K/C_3N/BlueP for the bilayer-C_3N/BlueP heterostructure, and C_3N/BlueP/BlueP/K > C_3N/BlueP/K/BlueP > C_3N/K/BlueP/BlueP > K/C_3N/BlueP/BlueP for the C_3N/bilayer-BlueP heterostructure. This implies that for the adsorption of more than one ion, the exterior of the BlueP layer will be filled first, followed by its other side. The next candidates for adsorption of more than one K ion are also summarized in Table 1. The calculated adsorption energies are lower than the BlueP monolayer's adsorption energy of −1.54 eV when used as anodes for KIBs.[4] As a result, we expect to achieve a high capacity comparable to that of the BlueP monolayer (865 mA h g^{-1}) but with significantly improved electronic conductivity, which is essential for electrode materials.

According to the calculated adsorption energies, the K ion and the exterior of the C_3N/BlueP and bilayer-C_3N/BlueP heterostructures have a similar binding strength (−1.6 eV), which is weaker than that of the C_3N/bilayer-BlueP heterostructure (−1.8 eV). These are consistent with the

calculated charge transfers, indicating that the K ion transfers more electrons to the C_3N/bilayer-BlueP heterostructure than to the C_3N/BlueP or bilayer-C_3N/BlueP heterostructure (0.85 vs 0.84). Therefore, the bond formed between the K ions and outside the BlueP layer is expected to be stronger in the C_3N/bilayer-BlueP heterostructure than in the other two heterostructures. These results correlate with the number of electrons transferred between layers even before the K-ion adsorption. As discussed previously, the C_3N/bilayer-BlueP heterostructure induced a charge transfer of 0.192 electrons between the layers, whereas the C_3N/BlueP and bilayer-C_3N/BlueP heterostructures induced a charge transfer of 0.133 electrons. Therefore, a higher charge transfer between the layers before K-ion adsorption indicates stronger binding between K ions and the substrates after K-ion adsorption.

Figure 3 shows the charge density difference contours over the adsorption sites with maximum and minimum charge transfers from the K ion to the substrates. According to these plots, the charge-depleted regions are close to the K ion, and the charge-accumulated regions are near the substrates, implying a significant charge transfer from the K ion to the BlueP and C_3N layers of all three heterostructures. When the K ion is located outside the BlueP layer (Figure 3a,c,e), which is the most favorable adsorption site, the charge accumulated regions are mainly located near the BlueP layers. A minimal
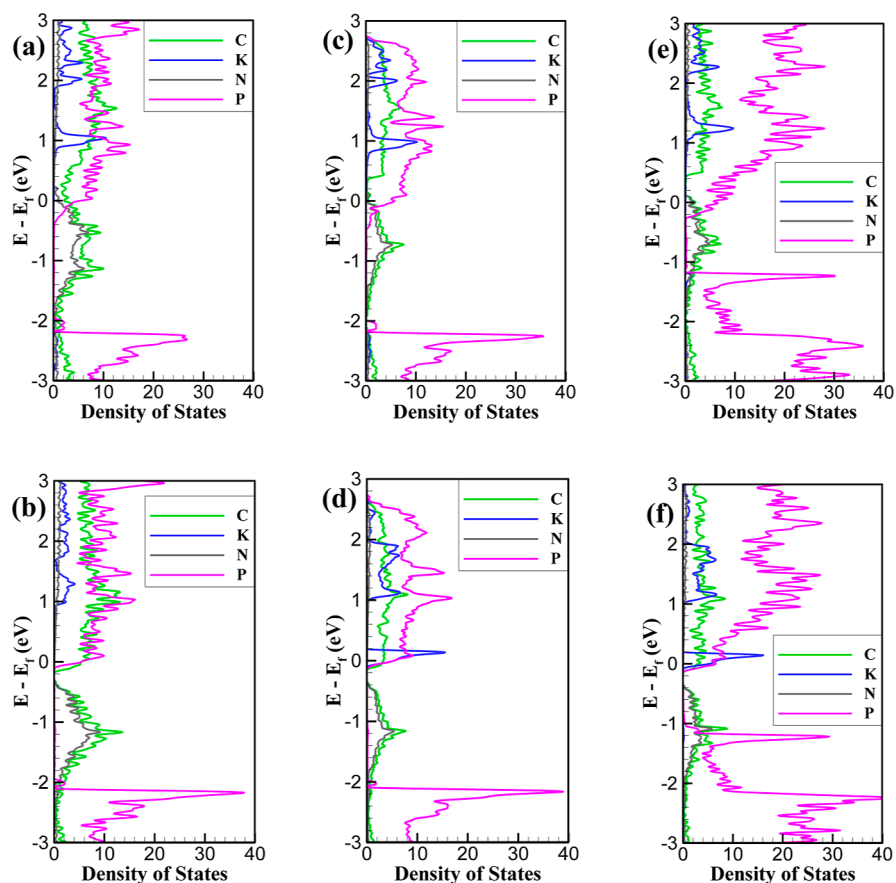
Figure 4. PDOS plots of the heterostructures with maximum and minimum charge transfers from one K-ion to (a,b) bilayer-C_3N/BlueP, (c,d) C_3N/BlueP, and (e,f) C_3N/bilayer-BlueP heterostructures.
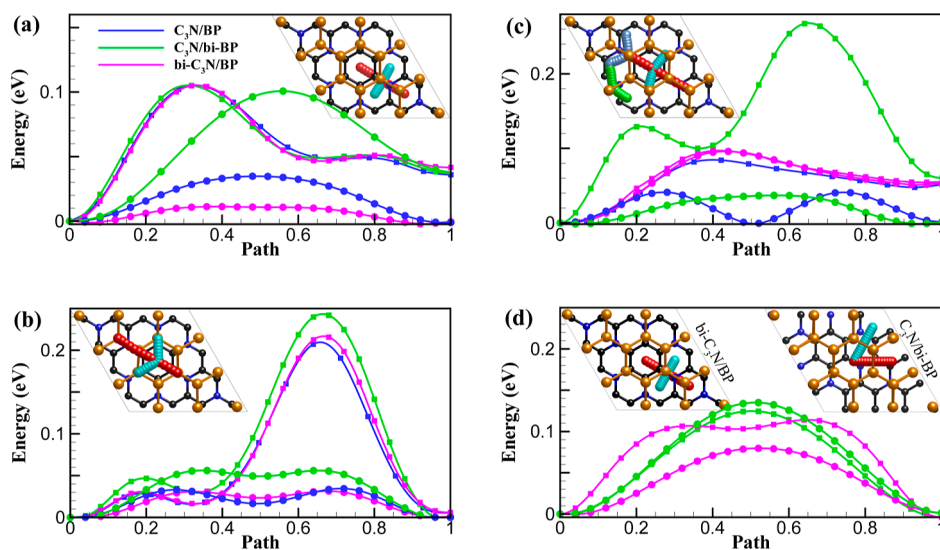
Figure 5. MEPs and the corresponding energy profiles of bilayer-C_3N/BlueP, C_3N/BlueP, and C_3N/bilayer-BlueP heterostructures for migration of K ions over (a) outside the C_3N layer, (b) outside the BlueP layer, (c) between the BlueP and C_3N layers, and (d) interface of the BlueP or C_3N bilayer.

charge accumulation is also observed near the C_3N layer of the C_3N/BlueP heterostructure. While the distance between the K-ion and the C_3N layer is the same in bilayer-C_3N/BlueP and C_3N/BlueP heterostructures, the former does not exhibit any indication of accumulated charges. This can be explained according to charge transfer calculations prior to K-ion

adsorption, as discussed in the previous section. We showed that the C_3N layer gained more charges at the interface of the C_3N/BlueP heterostructure than at the bilayer-C_3N/BlueP heterostructure interface, indicating its ability to attract more charges from the adjacent BlueP layer. On the other hand, when the K ion is adsorbed outside the C_3N layer, there are no

charge accumulation regions close to the BlueP layer. Moreover, when the K ion is adsorbed between the layers, the charge accumulates on both layers while the charge-depleted region is near the K ion. These plots and the calculated large charge transfers confirm the formation of a strong bond between the intercalant and the substrates.

Figure 4 illustrates the PDOS plots of the six aforementioned cases to further investigate the effect of the adsorption of a single K-ion on the electronic properties of heterostructures. The corresponding band structure plots are shown in Figure S4. According to the band structure plots of all cases, the Fermi level is pulled into the conduction band, resulting in significantly improved electronic conductivity compared with the pristine heterostructures. Additionally, maximum charge transfers from the K-ion to the substrates (cases a, c, and e) result in metallic behavior, as no bandgap is found. However, minimum charge transfers from the K-ion to the substrates (cases b−f) result in n-type semiconducting behavior. This is consistent with the PDOS plots, suggesting that the K-ion mainly contributed to the conduction bands as an n-doping element. Therefore, it implies the formation of bonds due to the charge carrier donation of the K-ion to the substrates, ultimately improving the electronic conductivity. Crystal orbital Hamilton population analyses, beyond the scope of this work, can provide a further understanding of the nature of crystal orbitals and the type of bonding and mechanism of electron transfer.[44,45]

3.4. Diffusion Properties of C₃N/BlueP Heterostructures. It is essential to investigate the diffusion energy barriers of the adsorbed atoms, as they influence the charge and discharge rates of batteries. These rates are correlated with ion diffusion barriers inside the anode material, as any adsorbed ion continuously migrates between the most stable sites along the minimum energy pathways (MEPs). If the diffusion barrier is sufficiently small for this migration, then the ion can migrate very quickly, which results in a high charge/discharge rate. However, a large diffusion barrier may lead to the irreversible trapping of K ions within the structure, resulting in severe structural distortions and low charge/discharge rates.

To investigate the diffusion energy barriers associated with K-ion migration over the heterostructures, we conducted CI-NEB simulations. Figure 5 illustrates the diffusion pathways and the corresponding energy profiles of a single K ion over bilayer-C₃N/BlueP, C₃N/BlueP, and C₃N/bilayer-BlueP heterostructures. Four different pathways are shown in this figure: (a) outside the C₃N layer, (b) outside the BlueP layer, (c) between the BlueP and C₃N layers, and (d) interface of the BlueP or C₃N bilayer. For each of these cases, we investigated the diffusion energy barriers in the zigzag and armchair directions, shown with circle and square symbols on the energy profiles, respectively. The following paths are included in panel (a): $H_{cn} \rightarrow H_c/H_{cn}$ along the armchair (red) and zigzag (cyan) directions; panel (b): $T_{pd} \rightarrow T_{pd}$ along the armchair (red) and zigzag (cyan) directions; panel (c): $T_{pu} \rightarrow T_{pu}$ along the armchair (red) and zigzag (cyan) directions of the C₃N/bilayer-BlueP, and $H_p \rightarrow H_p$ along the armchair (green) and zigzag (light blue) directions of the C₃N/BlueP and bilayer-C₃N/BlueP; panel (d): $H_p \rightarrow H_p$ along the armchair (red) and zigzag (cyan) directions of C₃N/bilayer-BlueP, and $H_{cn} \rightarrow H_c/H_{cn}$ along the armchair (red) and zigzag (cyan) directions of bilayer-C₃N/BlueP.

The calculated diffusion energy barriers indicate that the K ion can migrate faster in the zigzag direction than in the armchair direction, with two exceptions in the C₃N/bilayer-BlueP heterostructure. The first exception is outside the C₃N layer (panel a), where diffusion energy barriers in the armchair and zigzag directions are almost identical. The second exception is the interface of the BlueP bilayer (panel c), where the K-ion migrates faster in the armchair direction than in the zigzag direction.

We observed that the minimum diffusion energy barriers of the bilayer-C₃N/BlueP, C₃N/BlueP, and C₃N/bilayer-BlueP exteriors (panels a and b for outside the C₃N and BlueP layers, respectively) range from 0.031 to 0.033, 0.011 to 0.035, and 0.056 to 0.101 eV, respectively. According to the literature, the diffusion energy barriers for K-ion migration outside the BlueP and C₃N monolayers are 0.05 and 0.07 eV, respectively.[4,5] Therefore, when a C₃N monolayer or bilayer is added to a BlueP monolayer, the diffusion energy barriers of the layer exteriors decrease significantly. However, if a BlueP bilayer is added to a C₃N monolayer, the diffusion energy barriers of the layer exteriors increase significantly.

Overall, the bilayer-C₃N/BlueP heterostructure displayed lower diffusion energy barriers than the C₃N/BlueP and C₃N/bilayer-BlueP heterostructures, except along the zigzag path of the BlueP and C₃N bilayer interfaces (panel c). The highest diffusion energy barriers are found between the BlueP and C₃N layers of C₃N/BlueP and bilayer-C₃N/BlueP (0.042 and 0.096 eV) and between the BlueP layers of C₃N/bilayer-BlueP (0.124 eV). Therefore, adding an extra C₃N or BlueP layer on top of the bilayer C₃N/BlueP heterostructure doubles or triples its diffusion energy barriers. It is worth mentioning that the computed diffusion energy barriers, especially for the bilayer heterostructure, are still low and comparable to those of other known 2D materials, which will be discussed in later sections.

3.5. Specific Capacity and Open Circuit Voltage Profile. The energy storage capacity of anode materials is one of the most important characteristics of rechargeable-ion batteries, as it determines the amount of energy delivered during operations. The capacity of the anode material is proportional to the number of metal ions adsorbed on the structure. Thus, we need to sequentially adsorb K ions on the heterostructures following the orders listed in Table 1 to determine the theoretical capacity of the heterostructures. This procedure is repeated if the adsorption energies remain negative, ensuring that the K ions are adsorbed spontaneously and do not form metal clusters.

In addition to the examination of negative adsorption energies, it is also essential to investigate structural distortions and the distance of the K ions from the layers. Structural distortions should be as small as possible to ensure a reversible electrochemical process; in large deformations, the bonds between atoms can be irreversibly broken or weakened, activating the degradation mechanisms. Furthermore, the distance of K ions from the layers is also crucial since there is a drastic decrease in charge transfers of K ions far from the layers, forming metal clusters. To evaluate this statement further, we compared the total charge transfers of one layer and two layers of K-ion adsorptions outside the BlueP layer in the C₃N/BlueP heterostructure. Figure S5 illustrates the optimized structures of one layer and two layers of K ions adsorbed on this heterostructure and their vertical distances from the BlueP layer. Our calculations revealed that the first layer of K ions yields a negative adsorption energy of −0.27 eV, and adding a second layer yields a negative adsorption energy

of −0.15 eV. However, the introduction of a second layer of K ions results in only a marginal increase of 0.7% in the total charge transfer when compared to the adsorption of the first layer. Therefore, the charge transfers of the adsorbed ions decrease sharply by increasing their vertical distance from the substrate (6.67 Å vs 2.65 Å). In other words, the adsorption of two layers of K ions on the C_3N/BlueP heterostructure does not lead to a notably larger release of electrons when compared to the adsorption of only one layer of K ions. This is consistent with those of previous studies. For example, Yang et al.[46] showed that adding a second layer of lithium ions on top of the C_4N monolayer resulted in almost the same number of electrons being transferred from the lithium ions to the substrate, while the calculated adsorption energies were still negative. Therefore, despite the fact that some studies have considered multilayer adsorption of various metal ions on the substrates solely based on the negative adsorption energies[47−49] we took a different approach by focusing on only one-layer adsorption to ensure large charge transfers.

Our simulations revealed that each side of the BlueP or C_3N layer can accommodate a maximum of 9 K ions.[4] Therefore, the C_3N/BlueP, bilayer-C_3N/BlueP, and C_3N/bilayer-BlueP heterostructures can accept a maximum number of 27, 36, and 36 K ions, respectively. Figure S6 shows the optimized heterostructures for different K-ion concentrations. It also illustrates the maximum volume expansions of the heterostructures. At the maximum concentration of K ions, the resulting volume expansions of bilayer-C_3N/BlueP, C_3N/BlueP, and C_3N/bilayer-BlueP heterostructures in the out-of-plane/in-plane direction are 49.81/2.84, 38.17/3.4, and 41.42/3.93%, respectively. Therefore, heterostructures containing BlueP or C_3N bilayers exhibit higher volume expansions than those containing monolayers. The reason is that the interlayer distance of BlueP or C_3N bilayers is smaller than that of the BlueP and C_3N interfaces, as discussed previously. In other words, the adsorption of large K ions at heterostructure interfaces is much more favorable than that at bilayer interfaces. These findings are consistent with a previous study,[50] which reported that upon K-ion intercalation, graphene, ZrS_2, and $ZrSe_2$ bilayers expanded by 57.17, 75.61, and 90.32%, respectively, while graphene/$ZrSe_2$ and graphene/ZrS_2 heterostructures expanded by 53.07 and 54.13%, respectively. It is worth mentioning that our calculated volume expansions are lower than those of the graphene/$ZrSe_2$ and graphene/ZrS_2 heterostructures and even those reported for K-ion adsorption on graphite (61%).[51] Despite these high-volume expansions, 2D heterostructures may not contain enough elastic energy to initiate and propagate cracks, meaning they should be more resistant to fractures than bulk materials.[52] Additionally, our results indicate that as the number of intercalated ions increases, the displacement of substrate atoms from their equilibrium positions increases, especially in the C_3N layer. In order to evaluate the stability of the heterostructures at the maximum concentration of K-ions, we conducted full geometry optimization simulations after the adsorbed ions. We observed no structural deformation in the heterostructures. Furthermore, the adsorption energy of K-ions at maximum concentrations of 27, 36, and 36 K ions in C_3N/BlueP, bilayer-C_3N/BlueP, and C_3N/bilayer-BlueP, respectively, remained negative, indicating the stability of these heterostructures.

Our calculations demonstrated that the specific capacities of the C_3N/bilayer-BlueP, bilayer-C_3N/BlueP, and C_3N/BlueP

heterostructures are 636.7, 710.4, and 755.5 mA h g^{-1}, respectively. As a result, a bilayer heterostructure has the highest theoretical capacity since its surface-to-volume ratio is smaller than that of a trilayer heterostructure. Smaller surface-to-volume ratios provide a more electrochemically active surface area, which can enhance ion and charge transfers. Thus, it is expected that as the number of layers increases, the storage capacity of the material decreases, which shows the potential of 2D materials to store more ions than bulk materials such as graphite. However, the capacity reduction rate is not similar between the bilayer-C_3N/BlueP and C_3N/bilayer-BlueP heterostructures because of the larger mass in the BlueP layer than in the C_3N layer.

The OCV is another critical property of the anode materials, as it determines the delivered voltages during operations. Figure 6 illustrates the OCV profiles of the bilayer and trilayer
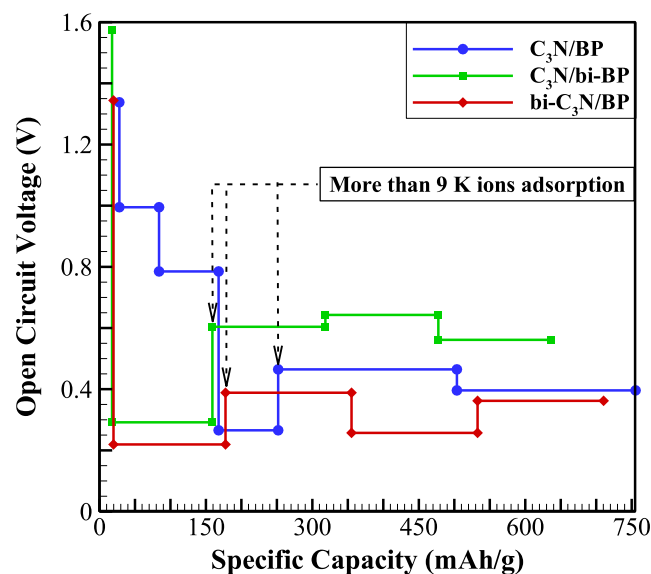
Figure 6. Open circuit voltage profiles of bilayer-C_3N/BlueP, C_3N/BlueP, and C_3N/bilayer-BlueP heterostructures with respect to the specific capacities.

C_3N/BlueP heterostructures versus their specific capacities, demonstrating that the lowest and highest OCVs belong to bilayer-C_3N/BlueP and C_3N/bilayer-BlueP, respectively. Therefore, the increased number of BlueP layers to C_3N layers increases the OCV values. Our calculations showed that the bilayer-C_3N/BlueP, C_3N/BlueP, and C_3N/bilayer-BlueP heterostructures have average OCVs of 0.33, 0.53, and 0.56 V, respectively. These values are in the range of suitable voltages (0.1−1 V) for anode materials, ensuring their good functionality as an anode material in KIBs. Additionally, Figure 6 shows that as soon as more than nine K ions are adsorbed on the heterostructures, the OCV sharply increases. The reason is that some atoms were adsorbed between the layers during the adsorption of more than nine K ions (panels b, f, and i in Figure S6), which increased the interlayer distance. This structural change substantially affects the OCV profiles.

3.6. Comparing the Capacity, Diffusion Barriers, and OCVs of Different 2D Heterostructures for KIBs,. In recent years, numerous theoretical studies have been conducted on 2D heterostructures as potential anode materials for KIBs. Even though the simulation techniques used in these

Table 2. Capacity, Diffusion Barriers, and OCVs of Different 2D Heterostructures Used as Anode Materials in K-Ion Batteries

electrode material	capacity (mA h g^{-1})	diffusion barrier (eV)	OCV (V)
C$_3$N/BlueP (this study)	755.5	0.042	0.53
bilayer-C$_3$N/BlueP (this study)	710.4	0.096	0.33
C$_3$N/bilayer-BlueP (this study)	636.7	0.124	0.56
C$_3$N/BlueP[47]	1007.63	0.07	0.2
graphene/ZrS$_2$[50]	727.6	0.07	0.46
GeSe/BlackP[53]	429.2	0.22	
graphene/ZrSe$_2$[50]	307	0.04	0.33
Ti$_2$CO$_2$/graphene[54]	209.8	0.22	0.75

studies do not have the same level of detail regarding simulation configurations, it is possible to compare the overall performance of the investigated materials by utilizing various electrochemical properties, such as capacity, diffusion energy barrier, and OCV. Table 2 summarizes the capacities, diffusion energy barriers, and OCVs of various materials used as anode materials in KIBs to provide a comprehensive understanding of the performance of bilayer and trilayer C$_3$N/BlueP heterostructures compared with other known 2D heterostructures.

According to Table 2, this study and a previous study[47] both reported the highest capacity for the bilayer C$_3$N/BlueP heterostructure. The main distinction between these two studies is the specific pseudopotentials used, along with the addition of trilayer C$_3$N/BlueP heterostructures in our research. While experiments are necessary to determine the optimal set of pseudopotentials for a specific material, it is widely accepted that PAW pseudopotentials are known to offer greater accuracy compared to ultrasoft pseudopotentials[55,56] which were utilized in the other study. Therefore, considering our utilization of PAW pseudopotentials, which resulted in differences of approximately 250 mA h g^{-1} in capacity and 0.03 eV in diffusion energy barriers, we anticipate our results to be more accurate than those of the other study. In addition, as opposed to the previous study's multilayer adsorption of K ions,[47] we only considered single-layer adsorption of K ions due to the drastic reduction in charge transfers of additional layers. The graphene/ZrS$_2$ heterostructure is the second-best material in terms of capacity[50] but its diffusion barrier value suggests that its overall performance is inferior to that of the C$_3$N/BlueP heterostructure, implying slower charge/discharge rates. The bilayer-C$_3$N/BlueP and C$_3$N/bilayer-BlueP heterostructures rank next in terms of capacity, but their diffusion barriers are higher than those of the C$_3$N/BlueP and graphene/ZrS$_2$ heterostructures. The C$_3$N/bilayer-BlueP is more likely than other high-capacity materials (>600 mA h g^{-1}) to irreversibly trap K ions during the charging/discharging process due to its high diffusion barriers. The bilayer-C$_3$N/BlueP has the lowest OCV value, making it suitable for higher voltage applications than for other 2D heterostructures.

The next rank of materials in terms of capacity belongs to the GeSe/BlackP heterostructure.[53] However, its high diffusion barrier makes it one of the least favorable materials. Although the graphene/ZrSe$_2$ heterostructure exhibits one of the lowest diffusion energy barriers, it fails to compete with the bilayer and trilayer C$_3$N/BlueP heterostructures due to its relatively low capacity.[50] Additionally, the Ti$_2$CO$_2$/graphene heterostructure exhibits the lowest reported capacity, a large diffusion energy barrier, and a high OCV, precluding it from competing with the bilayer and trilayer C$_3$N/BlueP heterostructures.[54]

4. CONCLUSIONS

This work provided additional evidence of the advantageous electrochemical properties of 2D C$_3$N/BlueP heterostructures for anode materials in KIBs. The calculated adsorption energies suggest that K ions are adsorbed spontaneously and stably on the C$_3$N/BlueP heterostructures. This work showed a significant number of electrons being transferred from the K ions to the substrates, consistent with the formation of strong bonds. Additionally, all bilayer and trilayer heterostructure configurations exhibited minor lattice deformations even at the maximum concentration of K ions. Notably, upon removal of the K ions, the substrate atoms re-establish their original positions, indicating excellent stability during the charging and discharging processes. The storage capacity of C$_3$N/BlueP (755.5 mA h g^{-1}) was found to be higher than those of bilayer-C$_3$N/BlueP (710.4 mA h g^{-1}) and C$_3$N/bilayer-BlueP (636.7 mA h g^{-1}), with the bilayer-C$_3$N/BlueP exhibiting the lowest open circuit voltage (0.33 V) among the heterostructures. The increased capacity, rapid charging/discharging rates, and enhanced electronic conductivity of C$_3$N/BlueP heterostructures make them potential high-performance anode materials for KIBs.

■ ASSOCIATED CONTENT

ⓢ Supporting Information

The Supporting Information is available free of charge at https://pubs.acs.org/doi/10.1021/acsomega.3c06076.

Relaxed structures of the C$_3$N and BlueP monolayers and different stacking orientations of the bilayer and trilayer C$_3$N/BlueP heterostructures; the electronic properties of the C$_3$N and BlueP monolayers; the electronic properties for one K-ion adsorption on the heterostructures; the optimized structures for different numbers of K-ion adsorption on the heterostructures; optimized structures of one and two layers of K-ion adsorption on the C$_3$N/BlueP heterostructures; polar plots of Poisson's ratios and Young's moduli of bilayer-C$_3$N/BlueP, C$_3$N/BlueP, and C$_3$N/bilayer-BlueP heterostructures (PDF)

■ AUTHOR INFORMATION

Corresponding Author

Cristina H. Amon − *Department of Mechanical and Industrial Engineering, University of Toronto, Toronto, Ontario M5S 3G8, Canada; Department of Chemical Engineering and Applied Chemistry, University of Toronto, Toronto, Ontario M5S 3E5, Canada;* ⓞ orcid.org/0000-0003-4314-8120; Email: cristina.amon@utoronto.ca

Authors

Ali Khodadadi − *Department of Mechanical and Industrial Engineering, University of Toronto, Toronto, Ontario M5S 3G8, Canada;* ⦿ orcid.org/0000-0002-5023-8493

Akhil Kunjikuttan Nair − *Department of Mechanical and Industrial Engineering, University of Toronto, Toronto, Ontario M5S 3G8, Canada*

Carlos Manuel Da Silva − *Department of Mechanical and Industrial Engineering, University of Toronto, Toronto, Ontario M5S 3G8, Canada*

Complete contact information is available at:
https://pubs.acs.org/10.1021/acsomega.3c06076

Notes

The authors declare no competing financial interest.

■ REFERENCES

(1) Nathan, M. G. T.; Yu, H.; Kim, G.-T.; Kim, J.-H.; Cho, J. S.; Kim, J.; Kim, J.-K. Recent advances in layered metal-oxide cathodes for application in potassium-ion batteries. *Adv. Sci.* **2022**, *9*, 2105882.

(2) Sada, K.; Darga, J.; Manthiram, A. Challenges and prospects of sodium-ion and potassium-ion batteries for mass production. *Adv. Energy Mater.* **2023**, *13*, 2302321.

(3) Yao, X.; Huang, N.; Han, F.; Zhang, Q.; Wan, H.; Mwizerwa, J. P.; Wang, C.; Xu, X. High-performance all-solid-state lithium−sulfur batteries enabled by amorphous sulfur-coated reduced graphene oxide cathodes. *Adv. Energy Mater.* **2017**, *7*, 1602923.

(4) Mukherjee, S.; Kavalsky, L.; Singh, C. V. Ultrahigh storage and fast diffusion of na and k in blue phosphorene anodes. *ACS Appl. Mater. Interfaces* **2018**, *10*, 8630−8639.

(5) Bhauriyal, P.; Mahata, A.; Pathak, B. Graphene-like carbon−nitride monolayer: a potential anode material for na-and k-ion batteries. *J. Phys. Chem. C* **2018**, *122*, 2481−2489.

(6) Dong, Y.; Xu, Y.; Li, W.; Fu, Q.; Wu, M.; Manske, E.; Kröger, J.; Lei, Y. Insights into the crystallinity of layer-structured transition metal dichalcogenides on potassium ion battery performance: a case study of molybdenum disulfide. *Small* **2019**, *15*, 1900497.

(7) Nair, A.; Da Silva, C.; Amon, C. Tuning the adsorption and diffusion capabilities of titanium disulfide monolayers by doping and strain engineering: Implications for lithium-ion batteries. *Appl. Surf. Sci.* **2022**, *600*, 154164.

(8) Nair, A.; Da Silva, C.; Amon, C. Dopant-enhanced sodium and potassium-ion adsorption and diffusion in two-dimensional titanium disulfide. *J. Appl. Phys.* **2023**, *133*, 064302.

(9) Wu, Y.; Xu, Y.; Li, Y.; Lyu, P.; Wen, J.; Zhang, C.; Zhou, M.; Fang, Y.; Zhao, H.; Kaiser, U.; et al. Unexpected intercalation-dominated potassium storage in ws 2 as a potassium-ion battery anode. *Nano Res.* **2019**, *12*, 2997−3002.

(10) K Nair, A.; Da Silva, C.; Amon, C. Enhanced alkali-ion adsorption in strongly bonded two-dimensional tis2/mos2 van der waals heterostructures. *J. Phys. Chem. C* **2023**, *127*, 9541−9553.

(11) Wu, Y.; He, C.; Zhang, W. Building up a general selection strategy and catalytic performance prediction expressions of heteronuclear double-atom catalysts for n2 reduction. *J. Energy Chem.* **2023**, *82*, 375−386.

(12) He, C.; Ma, J.; Wu, Y.; Zhang, W. Design of novel transition-metal-doped c4n4 as highly effective electrocatalysts for nitrogen fixation with a new intrinsic descriptor. *J. Energy Chem.* **2023**, *84*, 131−139.

(13) He, C.; Liang, Y.; Zhang, W. Design of novel transition-metal-doped c6n2 with high-efficiency polysulfide anchoring and catalytic performances toward application in lithium−sulfur batteries. *ACS Appl. Mater. Interfaces* **2022**, *14*, 29120−29130.

(14) He, C.; Han, F.; Zhang, W. The inse/g-cn van der waals hybrid heterojunction as a photocatalyst for water splitting driven by visible light. *Chin. Chem. Lett.* **2022**, *33*, 404−409.

(15) Zhu, Z.; Tománek, D. Semiconducting layered blue phosphorus: a computational study. *Phys. Rev. Lett.* **2014**, *112*, 176802.

(16) Zhang, J. L.; Zhao, S.; Han, C.; Wang, Z.; Zhong, S.; Sun, S.; Guo, R.; Zhou, X.; Gu, C. D.; Yuan, K. D.; et al. Epitaxial growth of single layer blue phosphorus: a new phase of two-dimensional phosphorus. *Nano Lett.* **2016**, *16*, 4903−4908.

(17) Zhou, X.; Feng, W.; Guan, S.; Fu, B.; Su, W.; Yao, Y. Computational characterization of monolayer c3n: A two-dimensional nitrogen-graphene crystal. *J. Mater. Res.* **2017**, *32*, 2993−3001.

(18) Liu, Q.; Xiao, B.; Cheng, J.-b.; Li, Y.-c.; Li, Q.-z.; Li, W.-z.; Xu, X.-f.; Yu, X.-f. Carbon excess c3n: a potential candidate as li-ion battery material. *ACS Appl. Mater. Interfaces* **2018**, *10*, 37135−37141.

(19) You, M.; Guo, G.; Luo, S.; Zhong, J. Rational design of a c 3 n/c 3 b p−n heterostructure as a promising anode material in li-ion batteries. *Dalton Trans.* **2023**, *52*, 2062−2072.

(20) Guo, G.-C.; Wang, R.-Z.; Ming, B.-M.; Wang, C.; Luo, S.-W.; Zhang, M.; Yan, H. C 3 n/phosphorene heterostructure: a promising anode material in lithium-ion batteries. *J. Mater. Chem. A* **2019**, *7*, 2106−2113.

(21) Lin, H.; Jin, R.; Zhu, S.; Huang, Y. C3n/blue phosphorene heterostructure as a high rate-capacity and stable anode material for lithium ion batteries: Insight from first principles calculations. *Appl. Surf. Sci.* **2020**, *505*, 144518.

(22) Bao, J.; Li, H.; Duan, Q.; Jiang, D.; Liu, W.; Guo, X.; Hou, J.; Tian, J. Graphene-like c3n/blue phosphorene heterostructure as a potential anode material for li/na-ion batteries: a first principles study. *Solid State Ionics* **2020**, *345*, 115160.

(23) Zhu, Y.; Wang, S.; Ma, J.; Das, P.; Zheng, S.; Wu, Z.-S. Recent status and future perspectives of 2d mxene for micro-supercapacitors and micro-batteries. *Energy Storage Mater.* **2022**, *51*, 500−526.

(24) Smith, J. B.; Hagaman, D.; Ji, H.-F. Growth of 2d black phosphorus film from chemical vapor deposition. *Nanotechnology* **2016**, *27*, 215602.

(25) Choi, J.-H.; Ha, M.-J.; Park, J. C.; Park, T. J.; Kim, W.-H.; Lee, M.-J.; Ahn, J.-H. A strategy for wafer-scale crystalline mos2 thin films with controlled morphology using pulsed metal−organic chemical vapor deposition at low temperature. *Adv. Mater. Interfaces* **2022**, *9*, 2101785.

(26) Jeon, W.; Cho, Y.; Jo, S.; Ahn, J.-H.; Jeong, S.-J. Wafer-scale synthesis of reliable high-mobility molybdenum disulfide thin films via inhibitor-utilizing atomic layer deposition. *Adv. Mater.* **2017**, *29*, 1703031.

(27) Tang, W.; Sanville, E.; Henkelman, G. A grid-based bader analysis algorithm without lattice bias. *J. Phys.: Condens.Matter* **2009**, *21*, 084204.

(28) Giannozzi, P.; Baroni, S.; Bonini, N.; Calandra, M.; Car, R.; Cavazzoni, C.; Ceresoli, D.; Chiarotti, G. L.; Cococcioni, M.; Dabo, I.; et al. Quantum espresso: a modular and open-source software project for quantum simulations of materials. *J. Phys.: Condens.Matter* **2009**, *21*, 395502.

(29) Perdew, J. P.; Burke, K.; Ernzerhof, M. Generalized gradient approximation made simple. *Phys. Rev. Lett.* **1996**, *77*, 3865−3868.

(30) Hamann, D. Optimized norm-conserving vanderbilt pseudo-potentials. *Phys. Rev.* **2013**, *88*, 085117.

(31) Grimme, S.; Antony, J.; Ehrlich, S.; Krieg, H. A consistent and accurate ab initio parametrization of density functional dispersion

correction (dft-d) for the 94 elements h-pu. *J. Chem. Phys.* **2010**, *132*, 154104.

(32) Fan, J.-Y.; Zheng, Z.-Y.; Su, Y.; Zhao, J.-J. Assessment of dispersion correction methods within density functional theory for energetic materials. *Mol. Simul.* **2017**, *43*, 568−574.

(33) Ganesh, P.; Kim, J.; Park, C.; Yoon, M.; Reboredo, F. A.; Kent, P. R. Binding and diffusion of lithium in graphite: quantum monte carlo benchmarks and validation of van der waals density functional methods. *J. Chem. Theory Comput.* **2014**, *10*, 5318−5323.

(34) Pfrommer, B. G.; Côté, M.; Louie, S. G.; Cohen, M. L. Relaxation of crystals with the quasi-newton method. *J. Comput. Phys.* **1997**, *131*, 233−240.

(35) Monkhorst, H. J.; Pack, J. D. Special points for brillouin-zone integrations. *Phys. Rev.* **1976**, *13*, 5188−5192.

(36) Kokalj, A. Computer graphics and graphical user interfaces as tools in simulations of matter at the atomic scale. *Comput. Mater. Sci.* **2003**, *28*, 155−168.

(37) Momma, K.; Izumi, F. Vesta 3 for three-dimensional visualization of crystal, volumetric and morphology data. *J. Appl. Crystallogr.* **2011**, *44*, 1272−1276.

(38) Taheri, A.; Da Silva, C.; Amon, C. H. Highly tunable thermal conductivity of c3n under tensile strain: A first-principles study. *J. Appl. Phys.* **2020**, *127*, 184304.

(39) Chen, P.; Zhang, Z.; Duan, X.; Duan, X. Chemical synthesis of two-dimensional atomic crystals, heterostructures and superlattices. *Chem. Soc. Rev.* **2018**, *47*, 3129−3151.

(40) Chen, Z.; Wang, H.; Li, Z. First-principles study of two dimensional c 3 n and its derivatives. *RSC Adv.* **2020**, *10*, 33469−33474.

(41) Ghosh, B.; Nahas, S.; Bhowmick, S.; Agarwal, A. Electric field induced gap modification in ultrathin blue phosphorus. *Phys. Rev.* **2015**, *91*, 115433.

(42) Born, M.; Huang, K.; Lax, M. Dynamical theory of crystal lattices. *Am. J. Phys.* **1955**, *23*, 474−475.

(43) Zhao, T.; Zhang, S.; Guo, Y.; Wang, Q. Tic 2: a new two-dimensional sheet beyond mxenes. *Nanoscale* **2016**, *8*, 233−242.

(44) Wu, Y.; He, C.; Zhang, W. "Capture-backdonation-recapture" mechanism for promoting n2 reduction by heteronuclear metal-free double-atom catalysts. *J. Am. Chem. Soc.* **2022**, *144*, 9344−9353.

(45) Wu, Y.; He, C.; Zhang, W. Novel design strategy of high activity electrocatalysts toward nitrogen reduction reaction via boron−transition-metal hybrid double-atom catalysts. *ACS Appl. Mater. Interfaces* **2021**, *13*, 47520−47529.

(46) Yang, C.; Zhang, X.; Ma, J.; Shi, B.; Zhang, H.; Xu, L.; Yang, J.; Liu, S.; Quhe, R.; Pan, F.; et al. Ultrahigh capacity of monolayer dumbbell c4n as a promising anode material for lithium-ion battery. *J. Electrochem. Soc.* **2020**, *167*, 020538.

(47) Ubaid, M.; Aziz, A.; Pujari, B. S. Two-dimensional c 3 n/blue phosphorene vdw heterostructure for li, na and k-ion batteries. *New J. Chem.* **2021**, *45*, 12647−12654.

(48) Wu, D.; Yang, B.; Chen, H.; Ruckenstein, E. New findings on an old question: Can defect-free graphene monolayers be superior metal-ion battery anodes? *Adv. Sustainable Syst.* **2020**, *4*, 1900152.

(49) Hu, J.; Liu, Y.; Liu, N.; Li, J.; Ouyang, C. Theoretical prediction of t-graphene as a promising alkali-ion battery anode offering ultrahigh capacity. *Phys. Chem. Chem. Phys.* **2020**, *22*, 3281−3289.

(50) King'ori, G. W.; Ouma, C. N.; Amolo, G. O.; Makau, N. W. Ab initio insights into graphene-zirconium disulfide/diselenide heterostructure as electrode material for alkali-ion batteries. *Surface. Interfac.* **2021**, *24*, 101036.

(51) Zhao, J.; Zou, X.; Zhu, Y.; Xu, Y.; Wang, C. Electrochemical intercalation of potassium into graphite. *Adv. Funct. Mater.* **2016**, *26*, 8103−8110.

(52) Androulidakis, C.; Zhang, K.; Robertson, M.; Tawfick, S. Tailoring the mechanical properties of 2d materials and heterostructures. *2D Mater.* **2018**, *5*, 032005.

(53) He, C.; Zhang, J. H.; Zhang, W. X.; Li, T. T. Gese/bp van der waals heterostructures as promising anode materials for potassium-ion batteries. *J. Phys. Chem. C* **2019**, *123*, 5157−5163.

(54) Demiroglu, I.; Peeters, F. M.; Gülseren, O.; Çakır, D.; Sevik, C. Alkali metal intercalation in mxene/graphene heterostructures: A new platform for ion battery applications. *J. Phys. Chem. Lett.* **2019**, *10*, 727−734.

(55) Taheri, A.; Da Silva, C.; Amon, C. H. First-principles phonon thermal transport in graphene: Effects of exchange-correlation and type of pseudopotential. *J. Appl. Phys.* **2018**, *123*, 215105.

(56) Borlido, P.; Doumont, J.; Tran, F.; Marques, M. A. L.; Botti, S. Validation of pseudopotential calculations for the electronic band gap of solids. *J. Chem. Theory Comput.* **2020**, *16*, 3620−3627.